7

Macroporous Silicon Photonic Crystals

A model system for 2D and 3D photonic crystals

Ralf B. Wehrspohn[1], Joerg Schilling[2]
[1]*Department of Physics, University of Paderborn, D-33095 Paderborn, Germany*
wehrspohn@physik.upb.de
[2]*California Institute of Technology, Pasadena, CA 91125, USA*
schill@caltech.edu

7.1. INTRODUCTION

From the beginning of research on photonic crystals, a major area of investigation concerned two-dimensional (2D) photonic crystals [1]. This was mainly caused by experimental reasons as the fabrication of 3D photonic crystals appeared to be more difficult and cumbersome than that of 2D photonic crystals. Additionally, the calculation of band structures for 2D photonic crystals is less time consuming and a lot of interesting phenomena (e.g., light localization—at least in a plane) can already be studied in 2D photonic crystals. However, an ideal 2D photonic crystal consists of a periodic array of infinitely long pores or rods so that the a structure which approximates this theoretical model has to exhibit very high aspect ratios (ratio between pore/rod length to pore/rod diameter). Using conventional dry etching techniques only structures with aspect ratios up to 10–30 are possible. To avoid the scattering of light out of the plane of periodicity and to reduce the corresponding loss the so-called slab structures were developed and thoroughly investigated [2,3]. In such low-aspect structures, one relies on the guiding of light by the total internal reflection in the third dimension and, consequently, deals with a full 3D problem. On the other hand, Lehmann and Grüning [4,5] as well as Lau and Parker [6] proposed macroporous silicon as a model system for 2D photonic crystals. This system consists of a periodic array of air pores in silicon. The pores are etched in hydrofluoric acid applying a photo-electrochemical dissolution process [7,8]. Using lithographic prestructuring the

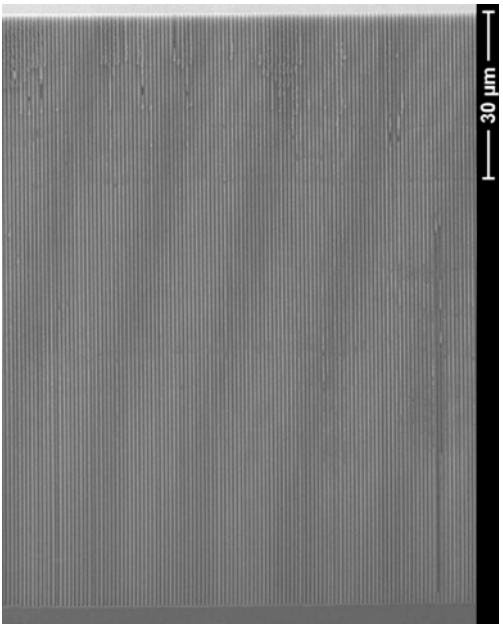

FIGURE 7.1. SEM image of a 2D trigonal lattice of macropores in silicon with a lattice constant of 0.7 μm. As the pore depth amounts to 100 μm the aspect ratio is >100 (courtesy of S. Schweizer).

nucleation spots of the pores can be defined at the surface of the n-type silicon wafer. This also allows us to control the pore pattern and its lattice constant. During the etching process the backside of the wafer must be illuminated to create electronic holes in the silicon which are consumed during the etching process. Due to the electrochemical passivation of the pore walls very high aspect ratios of 100–500 are obtained. As the fundamental band gap appears in general for wavelengths which are approximately twice the lattice constant, the pores are 50–250 times longer than the wavelengths of the corresponding 2D fundamental band gap. Therefore, macroporous silicon represents an excellent system to study ideal 2D photonic crystal properties. In Figure 7.1a structure with a triangular pore lattice with a lattice constant of $a = 700$ nm is shown. The pore depth is 100 μm. In the next paragraphs, optical experiments performed with such structures are presented and compared with calculations assuming a 2D array of infinitely long macropores. The lattice type and the pore depth of the investigated structures are the same as for the sample shown in Figure 7.1 while the interpore distance (lattice constant) and the diameter of the pores varies in order to meet the experimental requirements. Typically, high-quality photonic crystals with lattice constant of $a = 500$–8000 nm can be produced with this process. These structures exhibit photonic bandgaps from the near infrared (IR) to the far infrared.

7.2. 2D PHOTONIC CRYSTALS ON THE BASIS OF MACROPOROUS SILICON

7.2.1. Bulk Photonic Crystals

The dispersion relation for light propagation inside a photonic crystal is calculated using the plane wave method. Due to the 2D periodicity and the uniformity along the third

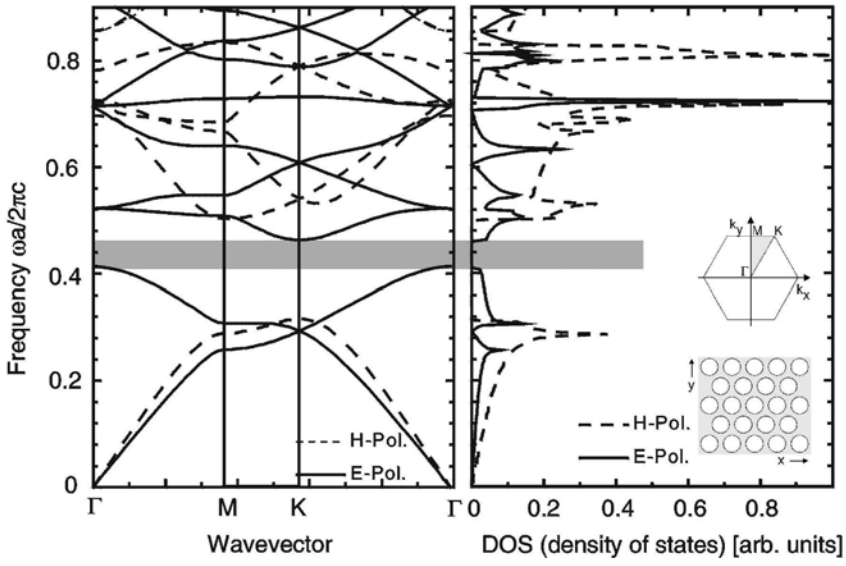

FIGURE 7.2. (a) 2D band structure of a trigonal macroporous silicon photonic crystal ($r/a = 0.45$). (b) Density of photonic states (DOS), inset: 2D hexagonal Brillouin zone and appropriate oriented trigonal pore lattice in real space. The grey bar indicates the 2D complete band gap. In this spectral range neither H-polarized nor E-polarized photonic states exist (DOS = 0) (courtesy of K. Busch).

dimension the light propagating in a 2D photonic crystal splits into E-polarized (E-field parallel to the pore axis) and H-polarized (H-field parallel to the pore-axis) waves. The band structures for these polarizations differ from each other and so do the bandgaps in width and spectral position. This originates in the different field distributions: Typically, the electric field of the H-polarized waves is located in the veins of the structures whereas the electric field of the E-polarized waves concentrates in the connection points of the veins. Figure 7.2a shows an example of a band structure for our system calculated for wave vectors in the first Brillouin zone along the path Γ–M–K–Γ. The assumed porosity or air filling factor is $p = 0.73$ which corresponds to $r/a = 0.45$ (r = pore radius, a = lattice constant) and the refractive index of silicon in the infrared is $n = 3.4$. For a triangular array of pores, a refractive index contrast exceeding 2.7 [9] and for suitable r/a ratios, the bandgaps for E- and H-polarizations overlap and a complete 2D photonic bandgap exists. As the refractive index contrast for air pores in silicon amounts to $n_{\mathrm{Si}}/n_{\mathrm{Air}} = 3.4$ in the IR, these requirements are fulfilled in our system. The band structure shown in Figure 7.2 thus exhibits such a complete bandgap indicated by a grey bar.

In addition to the band structure, the density of photonic states (DOS) is computed as well and presented in Figure 7.2b [13]. In the spectral region of the complete photonic band gap the DOS is zero, such that the propagation of light in the plane of periodicity with these frequencies is completely forbidden in the photonic crystal. To verify these theoretical calculations, transmission measurements through bars of the macroporous silicon photonic crystals along Γ–M and Γ–K directions were carried out. For this purpose, bars containing [13] pore rows were cut out using a second lithographic step. The measurements were performed using a Fourier transform infrared spectrometer (FTIR) in the spectral range between 700 cm^{-1} and 7000 cm^{-1} (14.3–1.43 μm). Figure 7.3

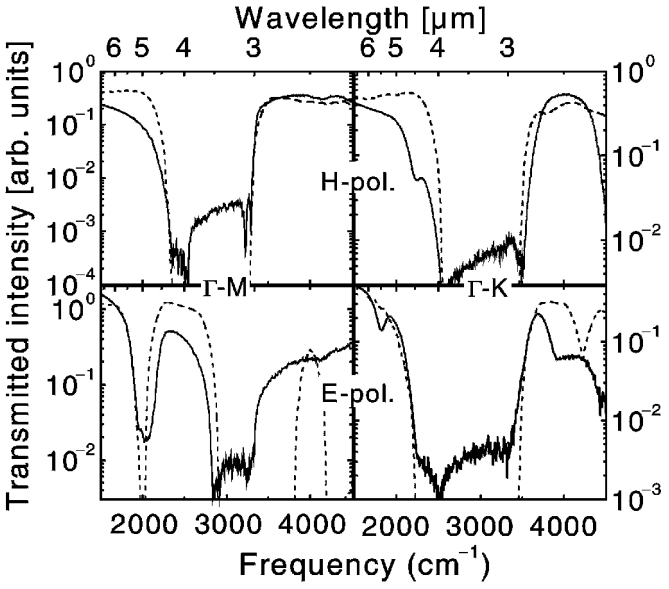

FIGURE 7.3. Transmission measurements (solid) and calculation (dashed) for penetration of a 2D macroporous silicon photonic crystal bar containing 13 pore rows. Transmission for both polarizations (*H*-polarization and *E*-polarization) along the two both high symmetry directions Γ–M and Γ–K are shown [13].

shows the measured spectra for both directions and both polarizations. They are compared to transmission calculations using the method developed by Sakoda [10]. The spectral positions of regions with vanishing transmission correspond well to the calculated spectrum. For the measurements along the Γ–M direction they can be attributed to the band gaps already discussed in Figure 7.2 for *H*-polarized and *E*-polarized light. However, the vanishing transmission in the range of 2200–3500 cm^{-1} for propagation along the Γ–K direction of *E*-polarized light cannot entirely be explained through a stop band. A comparison with the band structure of Figure 7.2 predicts a photonic band which covers the part of this spectral region. However, bands in which the experimentally incident plane wave cannot couple also lead to zero transmission [11,12]. These bands correspond to Bloch modes whose field distributions are antisymmetric with respect to the plane spanned by the pore axis and the direction of incidence. Consequently, although modes do exist in the photonic crystal they need not to be visible in transmission. Care has therefore to be taken when directly comparing reflection or transmission measurements with band structures: Although a band gap always leads to the total reflection/zero transmission, a spectral region exhibiting the total reflection/zero transmission does not necessarily coincide with a band gap. A direct comparison of experiment and theory is therefore rather based on reflection/transmission calculations than on band structure calculations alone. Beside the applied Sakoda method, mainly transfer matrix and finite difference time domain (FDTD) methods have been used for the calculation of reflection and transmission of macroporous silicon photonic crystals (Table 7.1.).

The complete band gap derived from band structure calculations comprises the interval between 2900 and 3300 cm^{-1} (3.44–3.03 μm). It clearly overlaps with all spectral

TABLE 7.1. Methods for the determination of the dispersion relation and the transmission/reflection of photonic crystals used in this work.

Method	Dispersion relation $\omega(k)$	Transmission $I(\omega)$	Reference.
Plane waves	Yes	No	[14]
Sakoda-plane waves	No	Yes	[10,12]
Transfer matrix	No	Yes	[15]
FD-TD	Yes	Yes	[16]

regions with vanishing transmission. The optimum band gap cannot be understood by Bragg scattering only. For scatterers whose spatial dimensions are comparable to the wavelength, additional scattering resonances (known as Mie resonances for spherical particles) appear. They depend on the size and shape of the scatterers. Consequently, apart from symmetry, lattice constant and refractive index, the radius of the pores (r/a-ratio) has an influence on the existence, the position and the width of the photonic band gaps. A graphic representation of the relationship between gap frequencies and filling ratio is known as a gap map, which for our structure, has been calculated before [13]. To verify this gap map experimentally, transmission measurements for 17 different samples spanning a wide range of r/a-ratios were carried out. The band edges were determined from these measurements and are compared with the theoretical predictions in Figure 7.4. The overall correspondence is very good. For lower r/a-ratios only a band gap for the H-polarization exists. A complete band gap only appears for $r/a > 0.4$ as then an E-band gap appears which overlaps with the H-band gap. With increasing r/a-ratios the E-band gap widens while the H-band gap shrinks for very high filling ratios. A maximum complete band gap of $\Delta\omega/\omega = 16\%$ for $r/a = 0.48$ can be deduced. This relatively large complete band gap is a consequence of the strong refractive index contrast between the

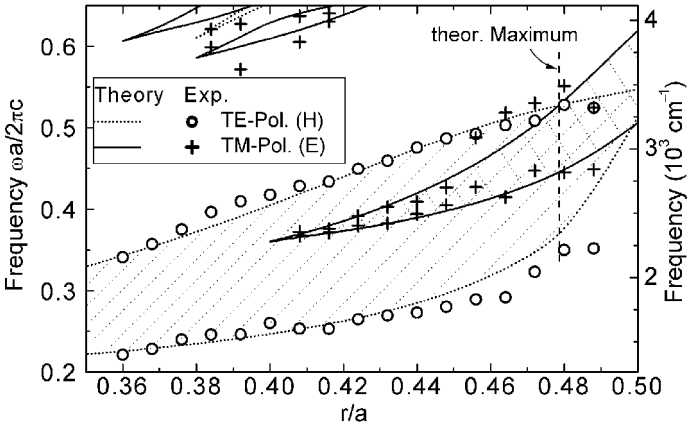

FIGURE 7.4. Position of the band gaps for H-polarized light (dotted) and E-polarized light (solid) for a 2D trigonal macroporous silicon photonic crystal depending on the r/a-ratio (gap map). A complete band gap appears as an overlap of the gaps for both polarizations and attains its maximum size for an r/a-ratio of 0.48 [13].

silicon (pore walls) and air (inside the pores) as well as the synergetic interplay of Mie resonance and Bragg scattering resonance.

7.2.2. Finite Photonic Crystals

Strictly speaking, the band structure calculations can only be performed assuming an infinitely extended photonic crystal. Therefore the band gap (zero DOS) also causing perfect total reflection only appears for infinite bulk photonic crystals. For a very thin bar of the photonic crystal the incident light of a frequency within the bulk band gap is no longer totally reflected. A certain amount can penetrate the thin photonic crystal. To investigate this effect four samples containing 1, 2, 3 and 4 crystal rows with an r/a-ratio of 0.453 were fabricated (Figure 7.5a). Transmission measurements for H-polarized light of different wavelengths along Γ–K were performed (see Figure 7.2) [17]. A tunable laser set-up was used which covered the spectral range between $3 < \lambda < 5$ μm corresponding to the range of the H-band gap ($3.1 < \lambda < 5.5$ μm) of the corresponding bulk photonic crystal. The experimental results were compared with transmission calculations applying the already mentioned Sakoda method with 4000 plane waves and revealed a very good agreement (Figure 7.5b). Plotting the transmittance versus the penetrated crystal thickness (Figure 7.5c) an exponential decay is observed. This corresponds to the

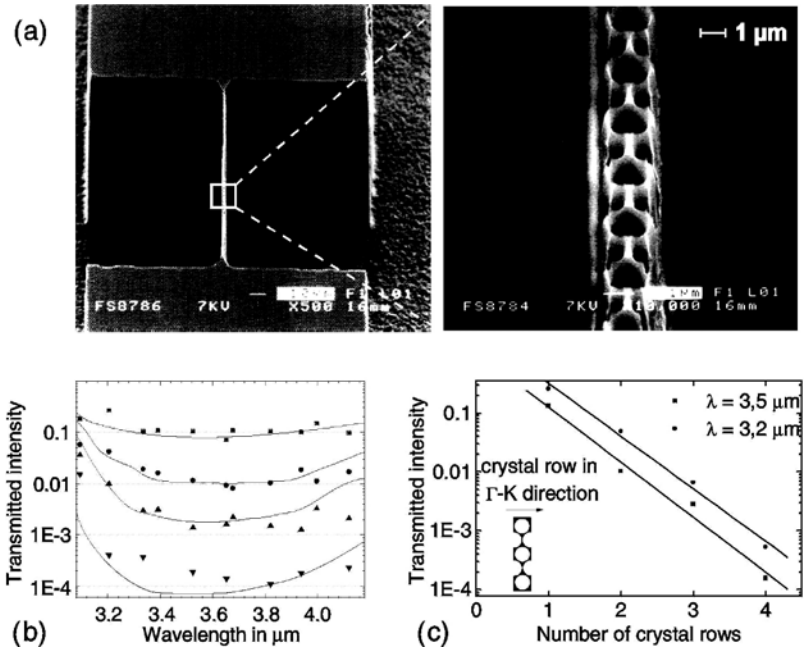

FIGURE 7.5. (a) SEM image of the macroporous silicon bars with varying width. The inset shows an enlarged view of the centre square. (b) Measured and calculated transmission for wavelengths within the H-band gap. Solid lines: Calculations for transmission through 1, 2, 3 and 4 crystal rows. Points: Measurements for 0.89 ± 0.04 (■), 1.8 ± 0.1 (●), 2.9 ± 0.1 (▲) and 4.2 ± 0.2 (▼) crystal rows (determined statistically). (c) Measured transmission as a function of bar thickness for two wavelengths within the band gap [17].

expectation that for frequencies within the band gap the light penetrating into the bulk photonic crystal is exponentially damped. The slope of the line in the logarithmic plot corresponds to a decay constant of 10 dB per crystal row for light with a wavelength near the centre of the band gap. Even for a bar containing only one pore row the band gap is already perceptible. This originates in the strong scattering of the single pores due to the large refractive index contrast between air pores and silicon walls.

7.2.3. Birefringence

In the first years of investigations in photonic crystals mainly the photonic band gap properties were studied. However, over the last years attention was also drawn to the other spectral regions of the dispersion relation that exhibit remarkable properties. For instance, the birefringence of a 2D macroporous silicon photonic crystal has been investigated in the spectral region below the first band gap. From theoretical investigations [18,19], it has been expected that a triangular 2D photonic crystal shows uniaxial properties for $\omega \to 0$. The optical axis coincides in this case with the pore/rod axis. For light propagating in this direction the effective refractive index is independent of the polarization direction (birefringence = 0). However, for light propagating in the plane of periodicity the 2D band structure reveals different slopes of the *E*- and *H*-polarized bands due to different mode distributions in the silicon matrix. This corresponds to different effective refractive indices for these two different polarizations and leads to birefringent behaviour of light propagation perpendicular to the pore axis. This effect was experimentally investigated in transmission using an FTIR spectrometer. The sample consisted of a macroporous silicon crystal with a lattice constant $a = 1.5\ \mu\text{m}$ and an r/a-ratio of 0.429. The transmission along Γ–M direction through a bar of 235 μm width containing 181 pore rows was measured [20]. In front of the sample a polarizer was placed and aligned with an angle of 45° relative to the pore axis. This defined a certain polarization state of the light incident on the photonic crystal and assured that the radiation consisted of *H*- and *E*-polarized components of comparable strengths. After penetration through the sample the beam passes through a second polarizer which was aligned parallel or perpendicular to the first polarizer, respectively. The measured transmission for parallel and crossed polarizers is shown in Figure 7.6. A periodic variation of the transmitted intensity is observed for both polarizer set-ups. The maxima of the parallel polarizer orientation correspond to the minima of the crossed orientation. This can be explained considering the phase difference which builds up between *E*- and *H*-polarized lights after penetration through the photonic crystal. This phase difference is given by $\Phi = 2\pi\,\Delta n_{\text{eff}} df/c$ (Δn_{eff} is the effective refractive index, d is the thickness of penetrated photonic crystal, f is the light frequency). For parallel orientations of the polarizers a maximum occurs for $\Delta\Phi = 2m\pi$ while a minimum appears for $\Delta\Phi = (2m + 1)\pi$. For the crossed polarizers the opposite is true. The light frequency and the order of the maxima and minima are determined from the transmission curve and with this the birefringence Δn_{eff} can be calculated. It is frequency dependent (Figure 7.6). However, over the entire investigated spectral range its value exceeds 0.3 and attains its maximum at the upper limit of the investigated range (at the lower band edge of the first *E*-gap). The largest birefringence measured amounts to 0.366 at a frequency $f = 0.209c/a$. With this it is by a factor of 43 larger than the birefringence of quartz.

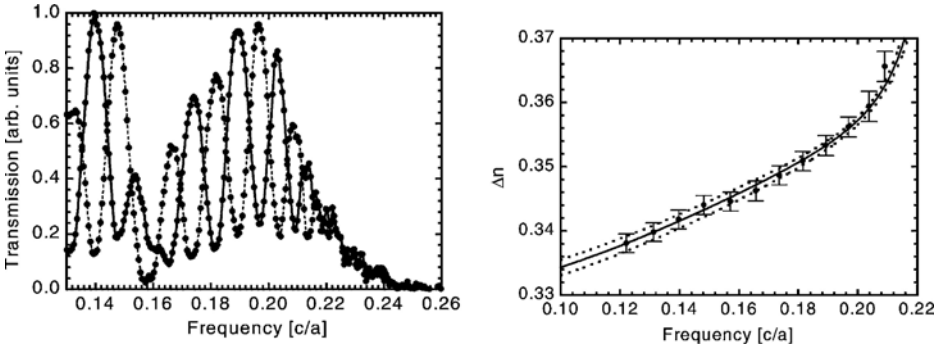

FIGURE 7.6. (Left) Effect of birefringence: measured transmission in the spectral range below the first band gap (long wavelength regime). Spectra were recorded for parallel (solid) and crossed (dashed) orientations of the two polarizers which were placed in front and behind the sample, respectively. The periodic maxima and minima in the transmission spectrum appear due to the phase difference between *E*- and *H*-polarized waves accumulating during penetration of the sample [20]. (Right) Spectral dependence of birefringence (Δn). Measurements (data points) and calculations (curves). The dashed curves represent the calculated dependence for the upper and lower bounds of the measured value of r/a (0.429± 0.002). The largest measured birefringence ($\Delta n = 0.365$) appears at the upper limit of the investigated spectral range close to the band edge for *E*-polarization [20].

The uniaxial behaviour of the triangular 2D photonic crystal in the limit $\omega \to 0$ corresponds to the well-known uniaxial birefringence of hexagonal atomic crystals in the visible. In atomic crystals the scatterers (atoms) have distances in the region of Å and therefore Bragg diffraction occurs for wavelengths in the x-ray region. For these classic atomic crystals, the visible region of the spectrum corresponds to the long wavelength limit $\omega \to 0$. In our case, where the lattice constant is of the order of 1 μm, Bragg diffraction occurs in the near- and mid-IR (causing the band gaps) while the limit $\omega \to 0$ comprises the long wavelength regions of the mid- and far-IR. In the described experiment only the birefringence along one propagation direction in the plane of periodicity was investigated. For the case of a uniaxial crystal this is sufficient, as the birefringence is constant for all propagation directions perpendicular to the optical axis. However, for increasing light frequencies which approach the first band gap this is no longer true. In this case, the value of the birefringence depends on the direction of propagation in the Γ–M–K-plane and the optical properties of the crystal can no longer be described by the terms "uniaxial" or "biaxial" known from classic crystal optics [21].

7.3. DEFECTS IN 2D MACROPOROUS SILICON PHOTONIC CRYSTALS

7.3.1. Waveguides

Since the beginning of the study of photonic crystals special attention was paid to intentionally incorporated defects in these crystals. Point or line defects can be introduced into macroporous 2D silicon photonic crystals by omitting the growth of a single pore or a line of pores. This can be achieved by designing a suitable mask for the lithography (the pattern defining process). To demonstrate waveguiding through a linear defect,

a 27 μm long line defect was incorporated along the Γ–K direction into a triangular 2D photonic crystal with an r/a-ratio of 0.43 ($r = 0.64$ μm) [22]. However, due to the photo-electrochemical fabrication process, the diameter of the pores, in the adjacent rows to the waveguide is increased.

The transmission through the line defect was measured with a pulsed laser source which was tunable over the whole width of the H-stop band in Γ–K direction ($3.1 < \lambda < 5.5$ μm). To couple light into the narrow waveguide (with a subwavelength width) with reasonable efficiency, a spatially coherent source of mid-IR light was used. A parametric source was used to produce a beam tunable from 3 to 6 μm, containing 200 fs pulses at a repetition rate of 250 kHz and a typical bandwidth of approximately 200 nm. The H-polarized beam was focused onto the sample by a 19 mm focal length ZnSe lens to a spot size of approximately 25 μm. Because the waveguide width was 1.1 μm, this spot size provided a theoretical coupling efficiency of approximately 4.8%. The transmitted light was passed through a monochromator, chopped, and detected with a pyroelectric detector and a lock-in amplifier. The transmission is defined as the ratio of the transmitted power to the total power incident upon the sample and is about 2%. The transmission deficit compared to 4.8% is attributed to the clipping of the beam by the substrate and diffraction as well as Fresnel losses.

The measured spectrum (Figure 7.7) exhibits pronounced Fabry–Perot resonances over a large spectral range which are caused by multiple reflections at the waveguide facets. Comparing the spectrum with an FDTD transmission calculation reveals very good agreement and the comparable finesse of the measured and calculated resonances indicate small losses inside the sample.

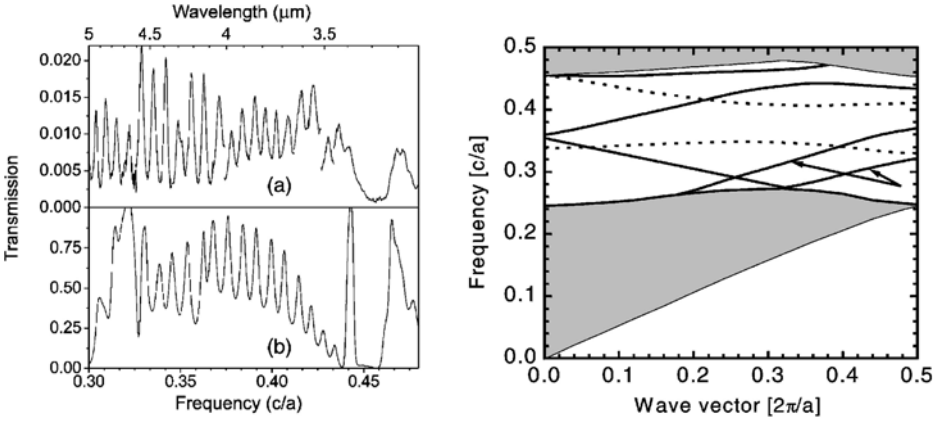

FIGURE 7.7. (Left) (a) Measured and (b) calculated H-polarized transmission spectrum of a 27 μm long waveguide directed along Γ–K covering the spectral range of the H-band gap of the surrounding perfect photonic crystal. The transmission is in %. Only the even waveguide modes contribute to the transmission as the incoming plane wave cannot couple to the odd waveguide modes. The small stop gap at a frequency of 0.45 c/a is caused by the anticrossing of two even waveguide modes [22]. (Right) Computed H-polarized band structure of the waveguide oriented along Γ–K. Solid and dotted curves correspond to even and odd modes, respectively. The two bands which are labelled with arrows appear due to the overetched pores on either side of the waveguide. The shaded areas correspond to the modes available in the adjacent perfect crystal regions [22].

A band structure calculation for H-polarization along Γ–K including waveguide modes is depicted in Figure 7.7. Here, the 2D band structure has been projected onto the new 1D Brillouin zone in Γ–K direction, since the line waveguide reduces the symmetry. The grey-shaded regions represent all possible modes inside the perfect crystal areas adjacent to the line defect. Defect modes bound to the line defect, therefore, occur only in the band gap, i.e., in the range $0.27 < f < 0.46$. They split into even and odd modes with respect to the mirror plane which is spanned by the waveguide direction and the direction of the pore axis. As the incoming wave can be approximated by a plane wave, the incident radiation can only couple to the even modes of the waveguide. The odd modes do not contribute to the transmission through the waveguide and, therefore, in this experiment transmission is solely connected with the even modes. The small stop band between the even modes around a frequency of 0.45 is reproduced as a region of vanishing transmission in Figure 7.7 due to anticrossing of the waveguide modes [23]. Furthermore, from the band structure it can be concluded that for $0.37 < f < 0.41\, c/a$ only a single even mode exists. Its bandwidth amounts to 10%.

7.3.2. Microcavities

Besides line defects also point defects, consisting only of one missing pore, are of special interest. Such a microresonator-type defect also causes photonic states whose spectral positions lie within the band gap of the surrounding perfect photonic crystal. The light fields belonging to these defect states are therefore confined to the very small volume of the point defect resulting in very high energy densities inside the defect volume. As the point defect can be considered as a microcavity surrounded by perfect reflecting walls, resonance peaks with very high Q-values are expected in the transmission spectra. Since the symmetry is broken in both high-symmetry directions, a band structure cannot be used anymore to describe point defect. To study this experimentally, a sample was fabricated including a point defect which was placed between two line defects serving as waveguides for coupling light in and out [24]. Figure 7.8 shows an SEM image of the described sample with an $r/a = 0.433$.

Measuring transmission through this waveguide–microresonator–waveguide structure demands an optical source with a very narrow line width. Therefore, a continuous wave optical parametric oscillator (OPO) has been used which is tunable between 3.6 and 4 μm and delivers a laser beam of 100 kHz line width. For spatially resolved detection an uncoated tapered fluoride glass fibre mounted to an SNOM head was applied and positioned precisely to the exit facet of the outcoupling photonic crystal waveguide (Figure 7.8). In the transmission spectrum two point defect resonances at 3.616 μm and 3.843 μm could be observed (Figure 7.9). Their spectral positions are in excellent agreement with the calculated values of 3.625 μm and 3.834 μm predicted by 2D-FDTD calculations taking into account the slightly widened pores surrounding the point defect. The measured point defect resonances exhibited Q-values of 640 and 190, respectively. The differences to the theoretical predicted values of 1700, 750 originate from the finite depth not considered in 2D calculations and the exact pore shape near the cavity. Recent 3D-FDTD calculations show that for high Q-values, the finite depth as well as the shape of the pores near the cavity play an important role in the determination of the Q-value [25]. Therefore, the 2D limit breaks for high-Q cavities under realistic conditions. Intuitively,

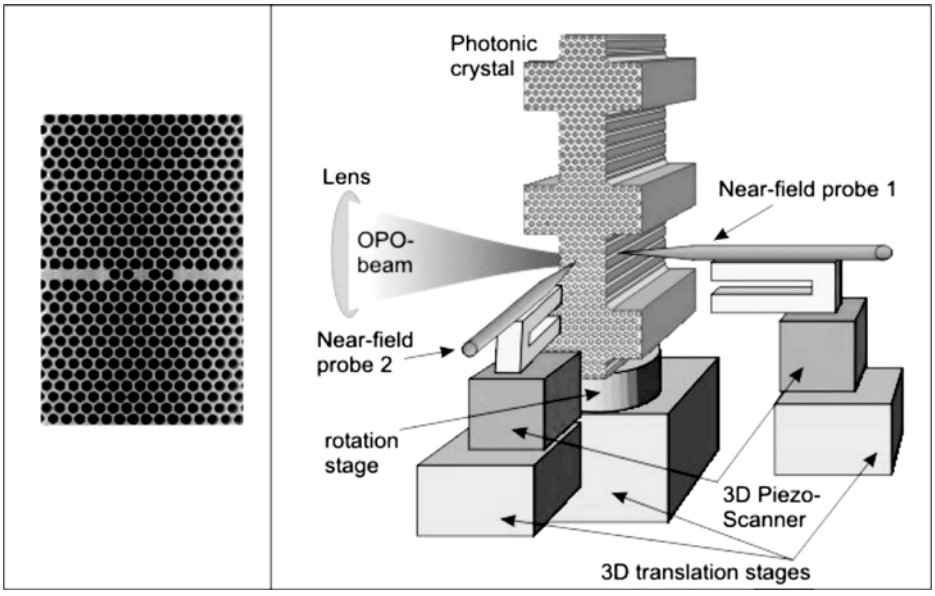

FIGURE 7.8. (Left) Top view of the photonic crystal region containing the waveguide–microresonator–waveguide structure. The r/a-ratio of the pores amounts to 0.433. The waveguides on the left and on the right serve to couple the light into the point defect (microresonator) [24]. (Right) Set-up of the optical measurement (courtesy of V. Sandoghdar).

this can be explained as follows. Any out-of-plane component of the incoming light will result in a spreading of the mode with depth and to a reduction of the Q-value. However, the reported high Q-values of this 2D microresonator might already be sufficient for studying the modification of radiation properties of an emitter placed in such a point defect.

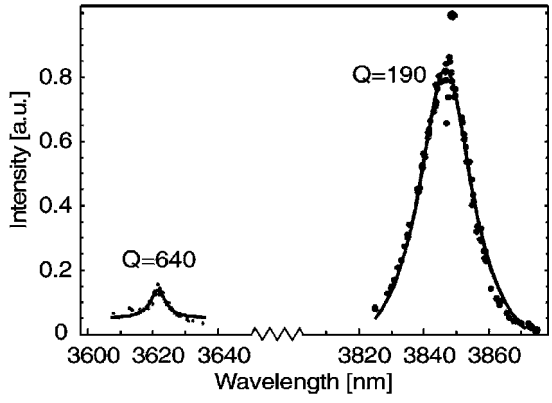

FIGURE 7.9. Measured monopole ($Q = 647$) and decapole resonances ($Q = 191$) of the point defect at wavelengths 3.616 μm and 3.843 μm [24].

7.4. 2D PHOTONIC CRYSTALS IN THE NIR

In the preceding paragraphs, experiments were reported which demonstrate the properties of macroporous silicon for 2D photonic crystals with band gaps in the mid-IR. Their high accuracy makes them a perfect model system to explore the concept of photonic crystals in the IR. Beside their physically interesting properties photonic crystals bear considerable potential for optical telecommunication (for instance, application of line defects for routing of the light beams). For these applications the photonic crystal waveguides have to work in a wavelength range between 1.3 μm and 1.5 μm so that they are compatible to the existing glass fibre network. This fact requires photonic crystals with band gaps in the corresponding spectral range. As it is known from Maxwell's equations, the spectral position of the band gap scales linearly with the lattice constant of the photonic crystals. Therefore, structures with sub-micrometre dimensions are necessary. Although they should not show a novel physical behaviour, their fabrication still is an experimental challenge. A triangular lattice was fabricated with a pitch $a = 0.7\,\mu\text{m}$ and an r/a-ratio of 0.365. To check the spectral position of the first-order band gap reflection measurements were performed using an IR microscope connected to an FTIR spectrometer. The reflection for H- and E-polarized lights incident in Γ–M direction was measured separately. A gold mirror was used as a reference. Figure 7.10 shows a comparison of the measured reflection spectra with the band structure. The grey-shaded spectral ranges represent the theoretically expected regions of high reflectivity stemming from the band gaps. They correspond very well to the experimental results. Although the reflected light contained contributions from beams with an incidence angle of up to 30° (due to the focussing conditions of the microscope), this off-normal incidence has only a

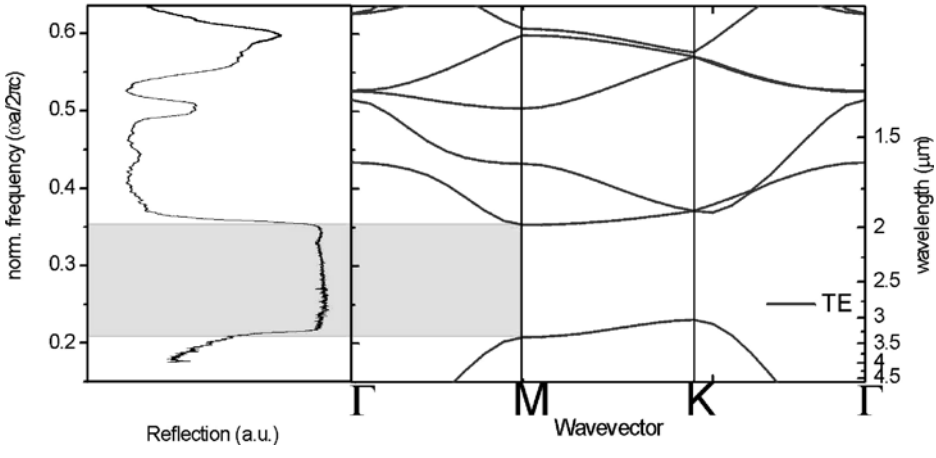

FIGURE 7.10. Reflectivity along Γ–M for a 2D trigonal macroporous silicon photonic crystal with a lattice constant of 0.7 μm for H-polarization (TE). Left: Measured reflectivity of a semi-infinite photonic crystal. Right: Comparison with band structure. Symmetric bands contribute to transmission while for asymmetric bands the incident plane waves cannot couple. Beside the band gaps they also cause total reflection. The dark-shaded range shows the fundamental band gap for H-Pol from 2 to 3.2 μm (courtesy of S. Richter).

negligible effect. The incident light is bent by refraction towards the normal propagating with a much smaller angular deviation inside the photonic crystal. Additionally, the width and position of this first-order band gap is not very sensitive for small angular deviations [26]. Please note that the very steep band edges reflect the very high quality of these structures which were obtained by a recently developed improved etching method. Also reflectivities originating from higher order band gaps, antisymmetric modes or modes with a low group velocity can be observed and are in very good agreement with the theory.

Together with the results of Schilling *et al.* and Rowson *et al.* who showed fundamental band gaps at 1.3 μm [27] and 1.5 μm [28], respectively, this experiment verifies that macroporous silicon structures can be fabricated and used as 2D photonic crystals for the technologically interesting telecommunication wavelengths between 1.3 and 1.5 μm. As was pointed out earlier, the attenuation for light frequencies within the band gap amounts to 10 dB per pore row. As Maxwell's equations scale with the structure size this relative property remains unchanged also for the down-scaled structure. This enables a close packing of waveguides, as the separation of 6–8 pore rows should be sufficient to avoid cross-talk between neighbouring waveguides.

In the last years, surface scattering is getting a more and more severe loss mechanism in III–V semiconductor-based photonic crystals. Silicon has in this sense a unique advantage. Scattering is supposed to originate form surface roughness inside the pores. High dielectric nano-roughness acts as the Mie scatterer for the light. However, high dielectric scatters inside the pores of a silicon photonic crystal can easily be converted to low dielectric scatterers by thermal oxidation. In Figure 7.11, the difference between an as-etched and an oxidized photonic crystal is shown for an extreme case. As-etched macroporous silicon shows in transmission almost no signal in the air band region. After a thin 10 nm oxide has been thermally grown, not only the transmission in the air band increases dramatically, it also enables Fabry–Perot resonances showing the very low losses [29].

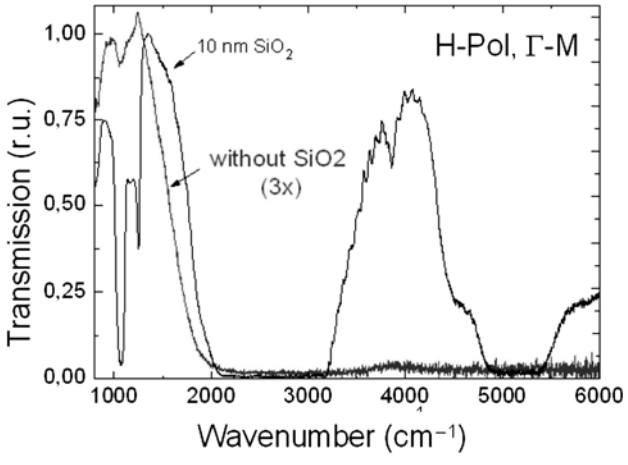

FIGURE 7.11. Effect of a thin oxide coating of the pores of an silicon photonic crystal. In grey, the transmission without the oxide coating is shown, in black the transmission with an oxide coating is shown [29].

7.5. TUNABILITY OF PHOTONIC BAND GAPS

7.5.1. Liquid Crystals Tuning

Small deviations of the fabricated experimental structures from designed ones have serious influence on their optical properties. In particular, the design of a microresonator (point defect) with a well-defined resonance frequency in the near-IR allows only fabrication tolerances in the sub-nanometre regime, a demand which currently cannot be fulfilled reproducibly. Additionally, for many applications, e.g., optical switches one would like to shift the band gap during operation. Therefore, tuning the optical properties during operation is a major point of interest. One way, to achieve this behaviour, is to change the refractive index of at least one material inside the photonic crystal. This can be obtained by controlling the orientation of the optical anisotropy of one material incorporated in the photonic crystal [30]. As the proof of the principle of the latter, a liquid crystal (E7 from EM Industries Inc.) was infiltrated into a 2D triangular pore array with a pitch of 1.58 μm and the shift of a band edge depending on the temperature was observed [31]. The liquid crystal E7 is in its nematic phase at room temperature but becomes isotropic at $T > 59\ ^{\circ}\mathrm{C}$. The refractive index for light polarized along the director axis is $n_e = 1.69$ while it is only $n_0 = 1.49$ for perpendicular polarization exhibiting a strong anisotropy.

Transmission for *H*-polarized light was measured along the Γ–K direction through a 200 μm thick bar of the infiltrated photonic crystal. In the case of room temperature, the first stop band of the *H*-polarization is observable in the range between 4.4 and 6 μm. Although a large band gap for the *H*-polarization still exists, the complete band gap, which is characteristic for the unfilled structure, is lost due to the lowered refractive index contrast within the infiltrated crystal. Therefore, the investigations were only carried out for *H*-polarization. When the structure is heated up, the upper band edge at 4.4 μm is red shifted while the lower band edge exhibits no noticeable shift. At a temperature of 62 °C the red shift saturates and the total shift amounts to $\Delta\lambda = 70$ nm as shown in Figure 7.12. This corresponds to 3% of the band gap width. The shift is caused by the change in the orientation of the liquid crystal molecules inside the pores. In a simplified model one can

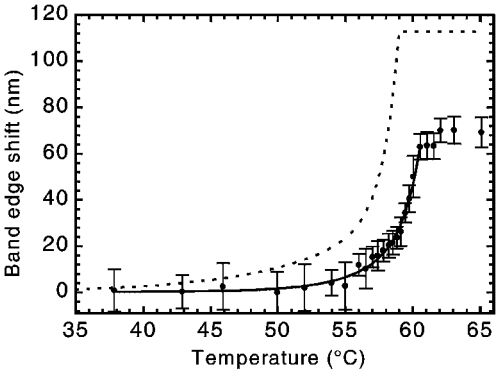

FIGURE 7.12. Temperature dependence of the band edge shift caused by temperature-induced phase transition of the infiltrated liquid crystal. Solid line: Fit to experimental data points. Dashed line: Calculation assuming a simple axial alignment of the liquid crystal in the pores [31].

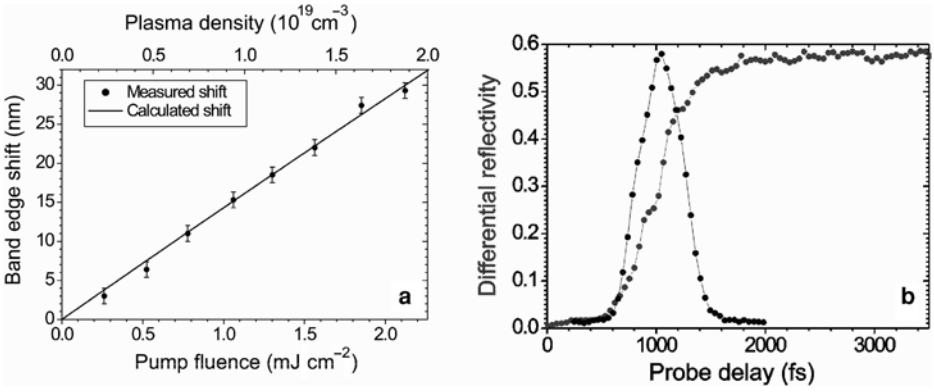

FIGURE 7.13. (a) Band edge shift as a function of the pump fluence, i.e., the plasma density. A maximum shift of 29 nm at 1.9 μm has been observed in good agreement with numerical calculations. (b) Transient behaviour of differential reflectivity at $\lambda = 1900$ nm for a pump beam at $\lambda = 800$ nm and a fluence of 1.3 mJ/cm^2. The band edge shift within 400 fs with a dynamic of 25 dB [32].

assume that all liquid crystal molecule directors line up parallel to the pore axis when the liquid crystal is in its nematic phase at room temperature. Then the *H*-polarized light (*E*-field in plane) sees the lower refractive index n_0 inside the pores. If the temperature is increased above 59 °C a phase transition occurs and the liquid crystal molecule directors are randomly oriented. The *H*-polarized light now sees a refractive index inside the pores which is an average over all these orientations. According to this model, a red shift of $\Delta\lambda = 113$ nm is expected which is slightly larger than the measured one. The difference in the observed and calculated shift is currently under investigation. Although the shifting or switching of a band gap via temperature is not very practical for a device, the present study confirms the possible tunability of photonic band gaps using liquid crystals.

7.5.2. Free-Carrier Tuning

Recently, ultrafast tuning of the band edge of a 2D macroporous silicon photonic crystals near 1.9 μm was shown [32]. In contrast to LQ switching, here the refractive index of the silicon matrix was tuned by the optical injection of free carriers. The photonic crystal was illuminated by laser pulse at $\lambda = 800$ nm, so well in the absorbtion region of silicon, with a pulse duration of 300 fs. The rise time of the change in the refractive index and thus the shift of the band edge was about 400 fs, slightly slower than the pulse due to the thermalization of the excited carrier (Figure 7.13). The band edge shift observed goes linearly with the pulse intensity as expected from Drude theory. For example, for a pump fluence of 2 mJ/cm^2, a band shift of 29 nm was observable. This is the fastest switching of 2D photonic crystals to date by free carriers.

7.6. 3D PHOTONIC CRYSTALS ON THE BASIS OF MACROPOROUS SILICON

Thus far, the main work based on macroporous silicon and photonic crystals concerned 2D photonic crystals. However, recently attempts have been undertaken to use

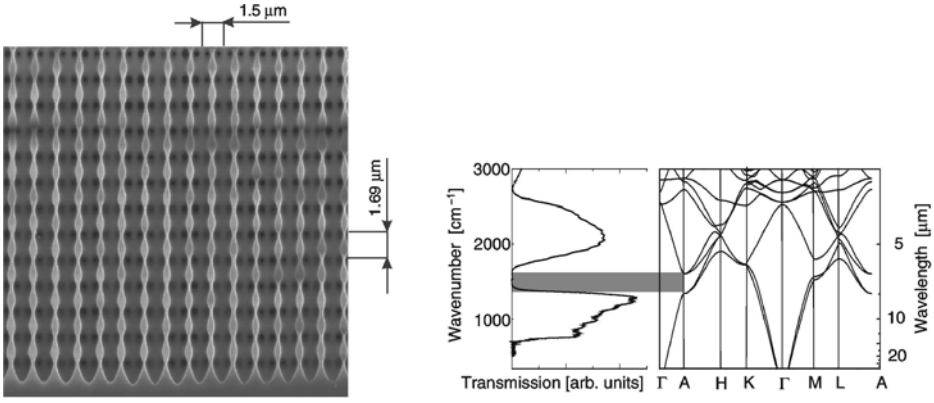

FIGURE 7.14. (Left) SEM image showing a longitudinal section of the modulated pore structure. The variation of the pore diameter with depth can be modelled by a sinusoidal modulation $r = r_0 + \Delta r \sin(2\pi z/l_z)$ with $r_0 = 0.63$ µm, $\Delta r = 0.08$ µm and $l_z = 1.69$ µm. [33]. (Right) Transmission measured in Γ–A-direction (along the pore axis) and comparison with calculated 3D band structure. The grey bar indicates the stop gap for light propagation in this direction causing transmission [33].

macroporous silicon for 3D photonic crystals. One approach to introduce a refractive index variation in the third dimension is the modulation of the pore diameter with pore depth [33]. As described in the first paragraph of this chapter, the pore diameter of the macropores can be controlled during the fabrication process (photo-electrochemical etch process) by the intensity of the backside illumination of the wafer. Strong illumination leads to high etching currents and, therefore, wide pores while the opposite is valid for low illumination.

The illumination intensity was now varied periodically during the etch process applying a zig-zag profile. Figure 7.14 shows an SEM image of a longitudinal section of the sample. The pore diameter modulation can be well approximated by a sinusoidal dependence on the pore depth. The modulation period amounts to 1.69 µm and the porosity varies between 81% and 49% between the planes of wide and narrow pore diameters. The lattice constant a of the 2D pore pattern is again 1.5 µm. The resulting 3D photonic crystal has a hexagonal lattice and the corresponding Brillouin zone has hexagonal shape too. Note that this is the first three-dimensional photonic crystal in the infrared region which perfectly extends over more than 10 lattice periods. To investigate the optical properties of the structure introduced by the pore diameter modulation, reflection measurements were performed along the pore axis which correspond to the Γ–A direction. The spectrum is shown in Figure 7.14 and compared to a 3D band structure calculation using the plane wave method. For comparison with the experiment, the most left part of the band structure shows the relevant dispersion relation along Γ–A. The stop gap in this direction caused by the periodic pore diameter modulation is indicated by a grey bar. It coincides well with the range of zero transmission between 1350 cm^{-1} ($\lambda = 7.41$ µm) and 1680 cm^{-1} ($\lambda = 5.95$ µm) measured along the pores.

Although the structure does not show a complete 3D bandgap it has another distinct property: As it is not based on building blocks of a fixed shape (e.g., spheres or

ellipsoids), the periodicity can be different for all directions. The modulation period along the pore axis (z-axis) can be independently controlled from the periodicity in the x–y-plane. Consequently, the dispersion relation along the pores can be adjusted nearly independently from the dispersion relation perpendicular to them. It turned out recently that the same structure but with an initial 2D cubic lattice does have a complete photonic band gap. The resulting structure is an inverted simple cubic lattice with a complete band gap of around 4% for realistic etching parameters [34].

Another approach to fabricate 3D photonic crystals on the basis of macroporous silicon includes a two-step process [35]. In the first step, a conventional 2D array of straight pores is photo-electrochemically etched. Afterwards additional pores are drilled under oblique angles from the top using a focused ion beam (FIB). In this way, a set of three different pore directions is established which cross each other in the depth. The fabricated structure is very similar to the well-known Yablonovite structure for the microwave region. However, a complete 3D band gap could not yet be shown experimentally as the angles between the three different pore sets have not been properly aligned. Another fabrication technique which should give a very similar result uses the photo-electrochemical etching of macropores on a (111) Si surface [36]. In contrast to the pore growth on a (100) Si surface, in the case of a (111) Si surface, the pores grow into ⟨113⟩-directions. As there are three equivalent ⟨113⟩ directions available from the (111) surface, three pores start to grow from each nucleation point at the surface. Band structure calculations for a corresponding structure show that the pores along the three ⟨113⟩ directions grow at suitable angles such that the structure should exhibit a 3D complete photonic band gap of about 7%. Very recently, different crystal structures with complete band gaps larger than 20% based on macroporous silicon have been predicted and are under current investigation [37].

7.7. SUMMARY

In summary, we have reviewed that macroporous silicon is a suitable material to fabricate ideal 2D photonic crystals for the IR. Due to the high refractive index contrast between silicon and air the band gaps are large and for a triangular array of pores a complete band gap for the light propagating in the plane of periodicity appears. Experimental investigations of such a structure for different porosities (r/a-values) confirm the calculated gap map and the maximum width of the complete band gap of 16% for an $r/a = 0.475$. The wide band gap of the H-polarization causes a strong attenuation for light with frequencies within the gap. The corresponding field is exponentially damped and a damping constant of 10 dB per pore row could be experimentally determined. Beside the band gaps also the long wavelength regime below the first band gap has been investigated. Large birefringence was experimentally and theoretically studied and a maximum value of $\Delta n_{\text{eff}} = 0.366$ (difference between H- and E-polarizations) was obtained which is by a factor of 43 larger than the birefringence of quartz. Due to the photolithographic prestructuring of the macroporous silicon, defects could intentionally be introduced. The transmission through a straight waveguide has been investigated. After comparison of the experimental features with band structure calculations a single-mode transmission in a spectral range with a bandwidth of 10% could be identified.

Additionally, transmission measurements at a point defect have been performed. Two resonances with Q-values of 647 and 191 were found and comparison with theory reveals that they can be attributed to the monopol and decapol mode of the microresonator. To obtain band gaps in the technologically interesting near-infrared spectral region, macroporous silicon 2D photonic crystals with structure sizes as small as $a = 0.5$ μm have been fabricated. They exhibit band gaps in the optical telecommunication window around $\lambda = 1.3$ μm which was confirmed by reflection measurements. Another issue, closely related to applications, is the tunability of photonic band gaps. A red shift of an upper band edge by 70 nm was demonstrated based on the refractive index change due to the reorientation of liquid crystals infiltrated into the pores. The reorientation was initiated by temperature change and corresponds to the phase transition nematic $\rightarrow$ isotropic of the liquid crystal. Moreover, for the first time the ultrafast switching (400 fs) of the band edge was shown by optically injected free carriers. This speed is compatible with packet switching in telecommunication technology. Finally perfect, extended 3D photonic crystals based on macroporous silicon were presented. Transmission measurements on these 3D photonic crystals with modulated pores showed good agreement with full 3D band structure calculations. Although these photonic crystals do not exhibit a complete 3D band gap the dispersion relation along the pores can almost independently be tuned compared to the dispersion relation perpendicular to it. In particular, one can imagine to utilize the mode structure of these or similar 3D photonic crystals based on macroporous silicon photonic crystals to realize novel atom traps. All these experiments show that macroporous silicon is an ideal material to study the properties of photonic crystals in the infrared regime as well as for possible technological applications operating in this spectral range.

ACKNOWLEDGEMENTS

This chapter is based on the results of a very fruitful collaboration with M. Agio, A. Birner, K. Busch, H.M. van Driel, F. Genereux, U. Gösele, R. Hillebrand, C. Jamois, S. John, P. Kramper, V. Lehmann, S.W. Leonard, J.P. Mondia, F. Müller, S. Richter, V. Sandoghdar, S. Schweizer, C. Soukoulis, and P. Villeneuve. We like to thank all of these. We gratefully acknowledge funding within the Schwerpunkt Programm "Photonische Kristalle" SPP 1113.

REFERENCES

[1] J.D. Joannopoulos, R.D. Meade and J.N. Winn, *Photonic Crystals*, Princeton University Press, New Jersey, 1995.
[2] S.G. Johnson, S. Fan, P.R. Villeneuve, J.D. Joannopoulos and L.A. Kolodziejski, Phys. Rev. B **60**, 5751 (1999).
[3] D. Labilloy, H. Benisty, C. Weisbuch, T.F. Krauss, R.M. De La Rue, V. Bardinal, R. Houdr, U. Oesterle, D. Cassagne and C. Jouanin, Phys. Rev. Lett. **79**, 4147 (1997).
[4] U. Grüning, V. Lehmann and C.M. Engelhardt, Appl. Phys. Lett. **66**, 3254 (1995).
[5] U. Grüning, V. Lehmann, S. Ottow and K. Busch, Appl. Phys. Lett. **68**, 747 (1996).
[6] H.W. Lau, G.J. Parker, R. Greef and M. Hölling, Appl. Phys. Lett. **67**, 1877 (1995).
[7] V. Lehmann and H. Föll, J. Electrochem. Soc. **137**, 653 (1990).
[8] V. Lehmann, J. Electrochem. Soc. **140**, 2836 (1993).

[9] R.D. Meade, K.D. Brommer, A.M. Rappe and J.D. Joannopoulos, Appl. Phys. Lett. **61**, 495 (1992).
[10] K. Sakoda, Phys. Rev. B **52**, 8992 (1995).
[11] W.M. Robertson, G. Arjavalingam, R.D. Meade, K.D. Brommer, A.M. Rappe and J.D. Joannopoulos, Appl. Phys. Lett. **61**, 495 (1992).
[12] K. Sakoda, Phys. Rev. B **52**, 7982 (1995).
[13] A. Birner, A.-P. Li, F. Müller, U. Gösele, P. Kramper, V. Sandoghdar, J. Mlynek, K. Busch and V. Lehmann, Mater. Sci. Semicond. Process. **3**, 487 (2000).
[14] K.M. Ho, C.T. Chan and C.M. Soukoulis, Phys. Rev. Lett. **65**, 3152 (1990).
[15] J.B. Pendry and A. McKinnon, Phys. Rev. Lett. **69**, 2772 (1992).
[16] A. Taflove, *Computational Electrodynamics: The Finite-Difference Time-Domain Method*, Artech House, Boston (1995).
[17] S.W. Leonard, H.M. van Driel, K. Busch, S. John, A. Birner, A.-P. Li, F. Müller, U. Gösele and V. Lehmann, Appl. Phys. Lett. **75**, 3063 (1999).
[18] A. Kirchner, K. Busch and C.M. Soukoulis, Phys. Rev. B **57**, 277 (1998).
[19] P. Halevi, A.A. Krokhin and J. Arriaga, Appl. Phys. Lett. **75**, 2725 (1999).
[20] F. Genereux, S.W. Leonard, H.M. van Driel, A. Birner and U. Gösele, Phys. Rev. B **63**, 161101(R) (2001).
[21] M.C. Netti, A. Harris, J.J. Baumberg, D.M. Whittaker, M.B.D. Charlton, M.E. Zoorob and G.J. Parker, Phys. Rev. Lett. **86**, 1526 (2001).
[22] S.W. Leonard, H.M. van Driel, A. Birner, U. Gösele and P.R. Villeneuve, Opt. Lett. **25**, 1550 (2000).
[23] H. Benisty, S. Olivier, M. Rattier and C. Weisbuch, in Photonic Crystals and Light Localization in the *21st Centruy*, Kluwer Academic Publishers, Dordrecht, 2001, pp. 117–128.
[24] P. Kramper, A. Birner, M. Agio, C. Soukoulis, U. Gösele, J. Mlynek and V. Sandoghdar, Phys. Rev. B **64**, 233102 (2001).
[25] M. Kafesaki and V. Sandoghdar, private communication (2003).
[26] S. Rowson, A. Chelnokov, C. Cuisin and J.-M. Lourtioz , J. Opt. A: Pure Appl. Opt. **1**, 483 (1999).
[27] J. Schilling, A. Birner, F. Müller, R.B. Wehrspohn, R. Hillebrand, U. Gösele, K. Busch, S. John, S.W. Leonard and H.M. van Driel, Opt. Mater. **17**, 7 (2001).
[28] S. Rowson, A. Chelnokov and J.M. Lourtioz, Electron. Lett. **35**, 753 (1999).
[29] A. Birner, *Dissertation*, University Halle, 2000.
[30] K. Busch and S. John, Phys. Rev. Lett. **83**, 967 (1999).
[31] S.W. Leonard, J.P. Mondia, H.M. van Driel, O. Toader, S. John, K. Busch, A. Birner, U. Gösele and V. Lehmann, Phys. Rev. B **61**, R2389 (2000).
[32] S.W. Leonard, H.M. van Driel, J. Schilling and R.B. Wehrspohn, Phys. Rev. B **66**, 161102 (2002).
[33] J. Schilling, F. Müller, S. Matthias, R.B. Wehrspohn and U. Gösele, Appl. Phys. Lett. **78**, 1180 (2001).
[34] S.W. Leonard, Appl. Phys. Lett. **81**, 2917 (2002).
[35] A. Chelnokov, K. Wang, S. Rowson, P. Garoche and J.-M. Lourtioz, Appl. Phys. Lett. **77**, 2943 (2000).
[36] M. Christophersen., J. Carstensen, A. Feuerhake and H. Föll, Mater. Sci. Eng. B **69–70**, 194 (2000).
[37] R. Hillebrand, S. Senz and W. Hergert, J. Appl. Phys. **94**, 2758 (2003).